Development and Evaluation of a MR Damper With Enhanced Effective Gap Lengths

GUOLIANG HU[ID], FENG YI, WANG TONG, AND LIFAN YU

School of Mechatronics and Vehicle Engineering, East China Jiaotong University, Nanchang 330013, China

Corresponding author: Guoliang Hu (glhu@ecjtu.edu.cn)

ABSTRACT Traditional magnetorheological (MR) damper featuring fixed gaps has the shortcomings of small damping force, single dynamic performance, and low adaptability. To overcome these shortcomings, a new MR damper with enhanced effective gap lengths is developed in this work, which achieves a double extension of the effective gap lengths via compactly integrating the conical fluid channels into the annular fluid channels. On the other hand, by altering the axial position of the valve spool controlled by a locking nut, the relative distance between the valve spool and piston of the MR damper is flexibly regulated; thus, the width of this adjustable gap in the conical fluid channels can be continuously adjusted. The magnetic circuit of the proposed MR damper is developed and its mechanical model is established as well to evaluate the dynamic performance. Sequentially, the finite element analysis (FEA) methodology is applied by using ANSYS/Emag software to investigate the changes of magnetic flux densities in these adjustable gaps. Moreover, a prototype is manufactured and experimental tests are conducted to verify its dynamic performance. The experimental results, under a fixed applied current, indicate that the damping force decreases with the increase of the adjustable gaps, and the maximum damping force reaches 7.2 kN at the adjustable gap of 0.6 mm. Besides, the dynamic range increases with the increase of the adjustable gap, and the dynamic range appears with a peak of 13.6. In addition, the damping force varies from 0.2 kN to 7.2 kN while the dynamic range attains 33 correspondingly by regulating the applied current and adjustable gap from 1.6 mm to 0.6 mm. From an experimental results perspective, the damping force and dynamic range can be not only effectively controlled by excitation current but also flexibly altered by regulating the width of the adjustable gaps simultaneously. Therefore, the dynamic performance of the proposed MR damper is also enhanced.

INDEX TERMS Magnetorheological damper, adjustable gaps, structural design, performance analysis.

I. INTRODUCTION

MR fluid is a smart material that mainly comprises carbonyl iron particles, carrier liquid, and some additives in a specific proportion [1]. The MR fluid can be transferred from ordinary newton-liquid state to solid state continuously and reversibly in milliseconds with or without magnetic fields, and its shear stress is related to the exerted magnetic field intensity [2], [3]. Due to its unique rheological properties, the MR fluid is widely employed in a variety of fields, such as bridges, buildings, vehicle suspensions, assistance orthoses, and robots [4], [5].

As a sort of typical semi-active actuating device, MR damper is successfully applied to various control systems

The associate editor coordinating the review of this manuscript and approving it for publication was Shunfeng Cheng.

owing to the utilization of MR fluid as a transmission medium. In general, MR dampers consist of the piston rod, piston head, excitation coil, and cylinder [6], [7]. With a magnetic field generated by the excitation coil, the MR fluid in the effective gap is rapidly energized to exhibit MR effect; thus, a damping force is promptly produced in the gap to weaken the vibration. Successive damping forces can be achieved by controlling the applied currents in the excitation coil [8], [9]. Therefore, MR damper possesses the merits of continuously controllable damping, fast response, low power consumption, and inexpensive cost [5], [10], [11].

To improve the dynamic performance of MR dampers, various significant researches have been studied on the structural design of MR dampers. By improving traditional MR fluid flow channels, Kim et al. [12] proposed an improved MR damper with a bifold flow mode, which is characterized by

connecting the inner and outer MR fluid flow channels with a feedback aperture on the magnetic core. It has been verified that this MR damper achieves a greater controllable damping force and equivalent damping. Liao *et al.* [13] designed a bypass MR damper featuring multi-stage radial channels. The multi-stage radial channels effectively extend the lengths of the gap and improve the utilization of the magnetic field. The experimental results manifest that the proposed MR damper possesses a better dynamic performance. Zemp *et al.* [14] presented a long-stroke MR damper by effectively prolonging the MR fluid channel and applied it to a 21-story building. Zhu *et al.* [15] developed a MR damper characterizing multiple fluid flow channels, by combining the annular and radial MR fluid flow channels, and the results reveal that the MR damper can provide a large damping force of 3.5 kN, which exhibits a good damping performance. Yazid *et al.* [16] constructed a hybrid-mode MR damper excited by five groups of excitation coil, which combines the shear mode with the extrusion mode of MR fluid. The experimental results demonstrate this MR damper yields a greater damping force than conventional MR dampers with a single-mode of MR fluid. Solomon *et al.* [17] designed a valve-mode MR damper for a six-axis MR prosthetic knee within a constrained length and radius. The finite element design via the response surface method was carried out to geometrically optimize this MR damper. Both the theoretical and experimental results show that the mass of this MR damper is reduced by 71% compared with a traditional MR damper; thus, it can be applied in those applications with small installation volume and short strokes. Cheng *et al.* [18] designed an MR damper with a magnetic winding and the damping force attained 3.4 kN under the sinusoidal velocity excitation with amplitude of 0.0628 m/s. To extend the effective gap length of the MR fluid channels, Hu *et al.* [19] proposed an improved MR damper on the premise of a restrained structural dimension, utilizing three non-conducting magnetic sleeves and four conducting magnetic sleeves to divide a single MR fluid flow channel into a serial-type MR fluid flow channel. The experimental results illustrate the peak damping force equals 6.8 kN and the equivalent damping coefficient reaches 290 kN/sm^{-1}.

The above methods to improve the dynamic performance of MR dampers primarily include: extending the MR fluid channels, changing the piston structures, optimizing magnetic circuits, and increasing the number of coils. From the structural principle point of view, these methods mentioned above only extended the effective gap lengths without regulating the width of effective gaps [20], [21]. Although the dynamic performance of these MR dampers has improved to some extent, some problems inevitably occur such as large structures, simple dynamic performance, and poor adaptability [22], [23]. As a highlight, the gap is one of the key parameters in designing MR dampers, and an appropriate gap can make MR dampers not only generate a greater damping force but also possess a larger dynamic range simultaneously [24], [25]. Zheng *et al.* [26] designed a novel multi-coil MR damper with a variable resistance gap

(VRG-MMD), which enables four electromagnetic coils with individual exciting currents. To obtain the optimal geometry of the proposed VRG-MMD, a multi-physics optimization including electromagnetics and fluid dynamics was conducted using Bound Optimization BY Quadratic Approximation (BOBYQA) technique. Though the multi coils achieve the extension of effective length that magnetic flux lines pass through, the axial dimension of VRG-MMD is inevitably increased and the variable resistance gap is only changed by the motion of piston rod but not flexibly adjusted according to the damping force requirement. Song *et al.* [27] investigated the effect of different MR fluid gaps on the braking performance of the MR brake. Verified by the theoretical analyses and experimental results, the braking torque increases with increasing the input current, and the difference for the impact of the gap exerts a huge effect on the braking torque under various input current. Phu *et al.* [28] proposed a new type of MR fluid mount featured by changeable gaps using a moved-plate valve structure, which is based on the flow mode and shear model of MR fluid. The main innovation of this MR fluid mount is the block-up behavior no longer occurs that may happen in conventional fixed plate mounts. However, due to only one excitation coil winding on the bobbin and simple magnetic circuit, the dynamic performance of the proposed MR fluid mount is not obviously enhanced compared with the conventional mount with the fixed gap. Kim *et al.* [29] presented a novel type of a tunable MR damper featured by permanent magnets, the damping force of which depends on the shape of the housing cylinder. The location of the permanent magnets that are connected to the moving piston varies with the magnetization area. The benefits of the proposed MR damper include no external power required to drive this damper, compact structures, higher cost-effectiveness, etc. Nevertheless, the damping force only controlled by the position of the piston is unable to meet the demand of practical damping force. To improve the dynamic performance of MR valves, Hu *et al.* [30] designed a new MR valve with a continuously tunable gap ranging from 1 mm to 2 mm. The adjustable range of the pressure drop varies from 470 kPa to 1150 kPa by tuning the resistance gap and applied current, which can replace a variety of MR valves featuring fixed gaps. Nonetheless, the main drawback of this MR valve lies in that the controllable pressure drop is still not sufficient for a great deal of application owing to the short effective gap length. It is also noted that moving parts frequently exist in those applications equipped with MR devices [31], [13]. Hence, the gap should be continuously adjustable while extending the effective length simultaneously, aiming to further boost the dynamic performance of MR dampers.

In terms of the aforementioned facts, the technical originality of this work is to propose a MR damper that extends the effective gap lengths and the gap of which can be flexibly adjusted simultaneously without restricted to the position of the piston rod, aiming to further boost the traditional MR damper with a single method to elevate its dynamic

performance. This paper presents a new MR damper with enhanced effective gap lengths, which achieves a double extension of the effective gap lengths via compactly integrating the conical fluid channels into the annular fluid channels. By altering the axial position of the valve spool controlled by the locking nut, the relative distance of the valve spool and the piston is flexibly regulated; thus, the adjustable gaps in the conical MR fluid channel can be continuously adjusted. The magnetic circuit is studied and its mechanical model is established as well. The FEA methodology is applied by using ANSYS/Emag software to validate the damping performance, and a series of experimental tests are also carried out to study the dynamic performance of the proposed MR damper.

II. STRUCTURAL DESIGN
A. STRUCTURAL PRINCIPLE
Fig. 1 and Fig. 2 portray the schematic configuration and photograph of the proposed MR damper with enhanced effective gap lengths, respectively. It is noted that the excitation coil is uniformly wound onto the piston which comprises the magnetic yoke I, conical sleeve, and magnetic yoke II. The chambers I, II, III filled with MR fluids are accordingly formed by the piston, non-magnetic sleeves, cylinder, and piston rod, respectively. The channels in which MR fluid flows between chamber I and II are represented as the conical fluid channels, and the channels between chamber I and III are denoted as the annular fluid channels.
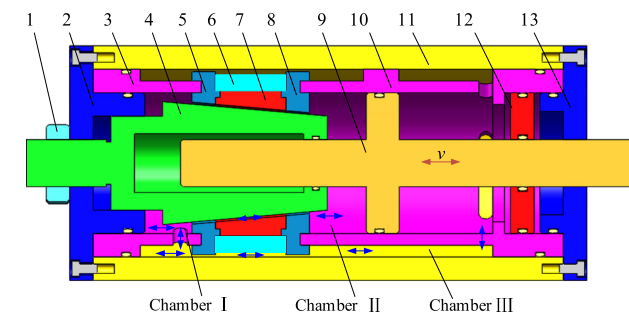
FIGURE 1. Schematic configuration of the proposed MR damper. (1) locking nut (2) end cover I (3) non-magnetic sleeve I (4) valve spool (5) magnetic yoke I (6) excitation coil (7) conical sleeve (8) magnetic yoke II (9) piston rod (10) non-magnetic sleeve II (11) cylinder (12) floating piston (13) end cover II.
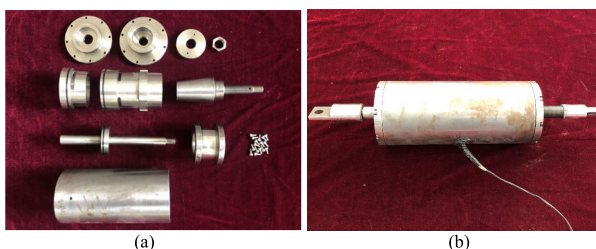

FIGURE 2. Photograph of the proposed MR damper: (a) Components and (b) Prototype.

In this design, the conical fluid channels with adjustable gaps are integrated into the annular fluid channels with fixed gaps. As a result, the proposed MR damper not only doubly extends the effective gap lengths but also is capable of continuously regulating these adjustable gaps in the conical fluid channels, thus significantly enhancing the dynamic performance of the proposed MR damper.

The locking nut is installed to adjust the axial position of the valve spool which can flexibly alter the adjustable gaps in the conical fluid channels. Specifically, when the locking nut is tightened clockwise, the valve spool axially moves to the right side to reduce the relative distance between the valve spool and piston. On the contrary, the valve spool horizontally shifts to the left side when the locking nut is unscrewed counterclockwise, thus augmenting the relative distance between the valve spool and piston. In this manner, the gap in the conical fluid channels can be continuously adjusted by regulating the locking nut. Thus, the damping force of the proposed MR damper can be directly alerted by regulating the width of adjustable gaps.

Fig. 3a and Fig. 3b respectively depict the distribution of the fluid channels under two particularly working modes, where the proposed MR damper operates with the maximum and minimum gap, respectively. When the extended length l of the valve spool comes up to l_{max}, the gap between the valve spool and piston reaches the maximum value h_{2max}. On the contrary, the adjustable gap accordingly attains the minimum value h_{2min} when extended length l is equal to l_{min}.
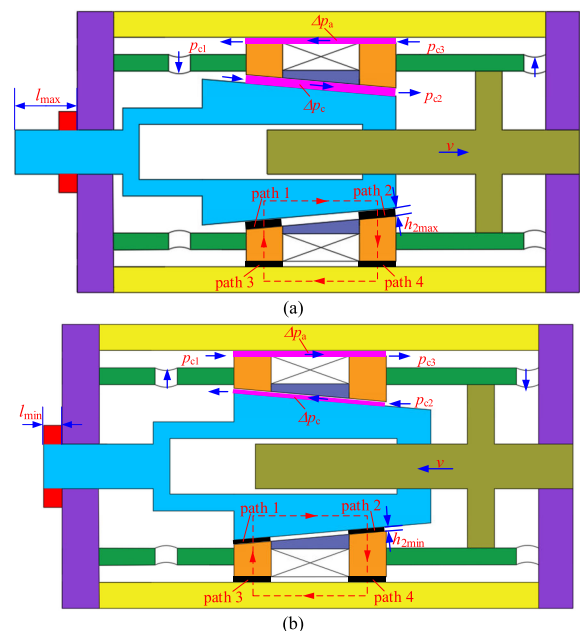
FIGURE 3. Distribution of fluid flow paths under two particularly working modes: (a) maximum gap h_{2max} and (b) minimum gap h_{2min}.

The adjustable gap in the conical MR fluid channels can be expressed by

$$h_2 = h_{2\,min} + (l - l_{min}) \tan\theta \cos\theta \approx h_{2\,min} + (l - l_{min})\theta \tag{1}$$

where h_2 is the adjustable gap in the conical fluid channels, $h_{2\max}$ and $h_{2\min}$ are the maximum and minimum values of h_2, respectively, l is the extended length of the valve spool, $l_{\max}$ and $l_{\min}$ are the maximum and minimum values of l, respectively, θ is the half cone angle of the conical fluid channels, it can be expressed as

$$\theta = \frac{h_{2\max} - h_{2\min}}{l_{\max} - l_{\min}} \quad (2)$$

External vibration drives the piston rod of the MR damper persistently moving back and forth along the axial direction. Here, the process of the piston rod moving to the right side is represented the stretching stroke (shown in Fig. 3a) while moving to the left side is acknowledged as the compression stroke (shown in Fig. 3b). With a direct current applied to the excitation coil, magnetic flux lines immediately begin with the valve core, then perpendicularly passes through the conical fluid channels, magnetic yoke I, annular fluid channels, cylinder, and the magnetic yoke II, ultimately returns to the valve spool to form a closed circuit. It is noted that the MR effect occurs in the conical and annular fluid channels simultaneously, namely paths 1, 2, 3, and 4 that the magnetic flux lines vertically pass through. To compensate the change of pressures p_{c1}, p_{c2}, and p_{c3} in chambers I, II, and III (shown in Fig. 3), the field-dependent shear yield stress comprising Δp_a in the annular fluid channels and Δp_c in the conical fluid channels is accordingly produced in paths 1, 2, 3, and 4 so that the MR damper generates damping force to suppress the external vibration. Therefore, with the adjustable gaps fixed, the damping force can be continuously adjusted by controlling the applied current. The specifications of the proposed MR damper are listed in Table 1.

TABLE 1. Specifications of the proposed MR damper.

Parameters	Values
Valve spool length (W)	50 mm
Magnetic yoke I length (w_1)	10 mm
Magnetic yoke II length (w_2)	10 mm
MR damper *radius* (r)	50 mm
Piston rod radius (r_1)	12.5 mm
Large-end radius (r_2)	26 mm
Small end radius (r_3)	19.86 mm
Groove depth of the piston (T)	8 mm
Cylinder thickness (D)	10 mm
Fixed gap (h_1)	1 mm
Adjustable gap (h_2)	0.6-1.6 mm
Half cone angle (θ)	5°
Coil turns (N)	670
Coil resistance (R)	3.36 Ω

B. MAGNETIC CIRCUIT ANALYSIS

Fig. 4 illustrates the magnetic circuit diagram of the proposed MR damper. Supposing there is no leakage in the magnetic circuit, the magnetic circuit can be analyzed using the Ohm's law, and it is expressed as

$$NI = \oint Hdl = R_m\phi \quad (3)$$

where N represents the number of turns of the excitation coil, I is the control current applied in the excitation coil, H is the magnetic field intensity, l is the length passed through by the magnetic flux lines, R_m is the total magnetic resistance of the magnetic circuit, and ϕ is the magnetic flux, which is deduced by

$$\phi = BS \quad (4)$$

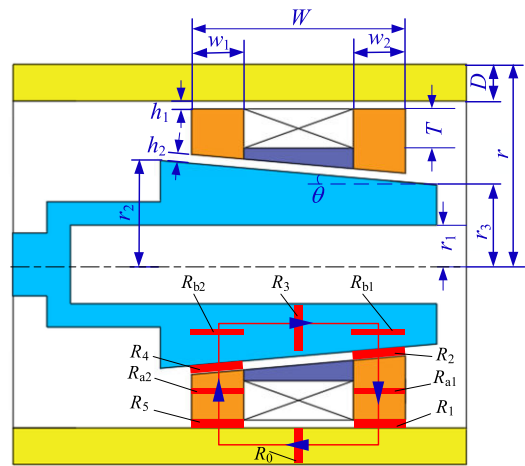where B denotes the magnetic flux density, and S represents the area passed through by the magnetic flux lines.

FIGURE 4. Simplified magnetic circuit.

The equivalent magnetic circuit of the proposed MR damper is depicted in Fig. 5. The total magnetic resistance can be expressed as

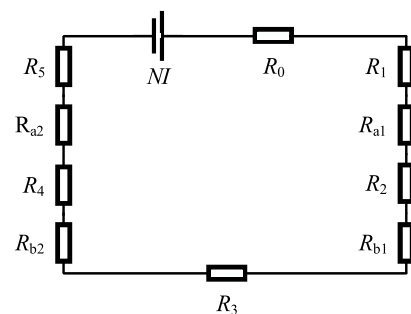$$R_m = R_0 + R_1 + R_{a1} + R_{b1} + R_2 + R_3 + R_4 + R_{a2} + R_{b2} + R_5 \quad (5)$$

FIGURE 5. Equivalent magnetic circuit.

The magnetic resistance of the cylinder is

$$R_0 = \frac{W - 0.5(w_1 + w_2)}{\pi[r^2 - (r - h_2/\cos\theta)^2]\mu_1\mu_3} \quad (6)$$

where W denotes the length of the valve spool, w_1 is the length of the magnetic yoke I, w_2 is the length of magnetic yoke II, r is the radius of the proposed MR damper, μ_1 is the relative magnetic permeability of #10 steel, and μ_3 is the magnetic permeability of free space, with a constant value of $4\pi \times 10^{-7}$ H/m.

The magnetic resistance of the MR fluid between the cylinder and magnetic yoke II can be represented as

$$R_1 = \frac{h_1}{2\pi[r - D - 0.5h_1]w_2\mu_2\mu_3} \quad (7)$$

where h_1 is the fixed gap, D is the thickness of the cylinder, μ_2 is the relative magnetic permeability of MR fluid.

The magnetic resistance of the magnetic yoke II and valve spool on the right side can be approximately added by

$$R_{a1} + R_{b1} = \frac{r - D - h_1}{\pi[r - D - h_1]w_2\mu_1\mu_3} \quad (8)$$

The magnetic resistance of the MR fluid between the magnetic yoke II and valve spool can be expressed as

$$R_2 = \frac{h_2}{2\pi[r_3 + 0.5h_2 + 0.5w_2 \tan\theta]w_2\mu_2\mu_3} \quad (9)$$

where r_3 is the small-end radius of the conical MR fluid channel.

The magnetic resistance of the valve spool is

$$R_3 = \frac{(W - 0.5(w_1 + w_2))^2}{\mu_1\mu_3 V} \quad (10)$$

where V is the effective volume of the valve spool, which can be calculated as

$$V = \frac{1}{3}\pi[W - 0.5(w_1 + w_2)][(r_3 - h_2 - 0.5w_1 \sin\theta)^2$$
$$+ (r_2 - h_2 + 0.5w_2 \sin\theta)^2$$
$$+ (r_3 - h_2 - 0.5w_1 \sin\theta)(r_2 - h_2 - 0.5w_2 \sin\theta)] \quad (11)$$

where r_2 is the large-end radius of the conical MR fluid channel.

The magnetic resistance of the MR fluid between the magnetic yoke I and valve spool can be represented as

$$R_4 = \frac{h_1}{2\pi[r_2 - 0.5h_2 + 0.5w_1 \tan\theta]w_1\mu_2\mu_3} \quad (12)$$

The magnetic resistance of the magnetic yoke I and the valve spool on the left side is approximately added by

$$R_{a2} + R_{b2} = \frac{r - D - h_1}{\pi[r - D - h_1]w_1\mu_1\mu_3} \quad (13)$$

The magnetic resistance of the MR fluid between the cylinder and magnetic yoke I is

$$R_5 = \frac{h_1}{2\pi[r - D - 0.5h_1]w_1\mu_2\mu_3} \quad (14)$$

Hence, the magnetic flux densities of MR fluid in paths I, III, IV, and VI that shown in Fig. 6 can be obtained as follows

$$B_{\mathrm{I}} = B_{\mathrm{II}} = \frac{NI}{2\pi[r_2 - 0.5h_2 + 0.5w_1 \tan\theta]w_1R_m} \quad (15)$$

$$B_{\mathrm{IV}} = \frac{NI}{2\pi[r - D - 0.5h_1]w_2R_m} \quad (16)$$

$$B_{\mathrm{VI}} = \frac{NI}{2\pi[r - D - 0.5h_1]w_1R_m} \quad (17)$$
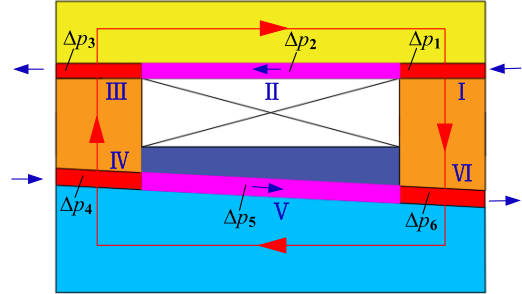

FIGURE 6. Schematic configuration of the distribution of pressure drop.

III. MATHEMATICAL MODEL

Fig. 6 depicts the distribution of the pressure drops of the MR damper under the exerted magnetic field. It is noted that the proposed MR damper operates in a valve model when a direct current is applied. The MR fluid in the annular fluid channels flow from path I to path III; subsequently, the MR fluid in the conical fluid channels flow from path IV to path VI. Therefore, four segments of effective gap lengths accordingly occur under the applied current, and the field-dependent pressure drop Δp is activated in paths I, III, IV, and VI. The total pressure drop Δp consisting of the field-dependent and viscosity pressure drops can be represented as

$$\Delta p = \Delta p_\eta + \Delta p_\tau = \Delta p_{a-\eta} + \Delta p_{a-\tau} + \Delta p_{b-\eta} + \Delta p_{b-\tau}$$
$$= \sum_{i=1}^{6} \Delta p_i = \sum_{i=1}^{6} \Delta p_{i-\eta} + \sum_{i=1}^{6} \Delta p_{i-\tau} \quad (18)$$

where Δp_η and Δp_τ are the total viscosity and field-dependent pressure drops, respectively; $\Delta p_{a-\eta}$ and $\Delta p_{a-\tau}$ are the viscosity and field-dependent pressure drops in the annular fluid channels, respectively; $\Delta p_{b-\eta}$ and $\Delta p_{b-\tau}$ are the viscosity and field-dependent pressure drops in the conical fluid channels, respectively; Δp_i is the pressure drop in i-th section of MR fluid channels; $\Delta p_{i-\eta}$ and $\Delta p_{i-\tau}$ are the viscosity and field-dependent pressure drop generated in the i-th section, respectively.

Supposing no magnetic flux lines passing through the middle gaps in annular and conical MR fluid channels, i.e. II and V, there is

$$\Delta p_{2-\tau} = \Delta p_{4-\tau} = 0 \quad (19)$$

According to the parallel plate model portrayed in Fig. 7, the shear rate u of MR fluid is given by [32]

$$u = \frac{\Delta p}{2\eta l}y^2 + \frac{\Delta ph}{2\eta l}y \quad (20)$$

where η is the viscosity of MR fluid without a magnetic field, l is the parallel plate length, y is the longitudinal position
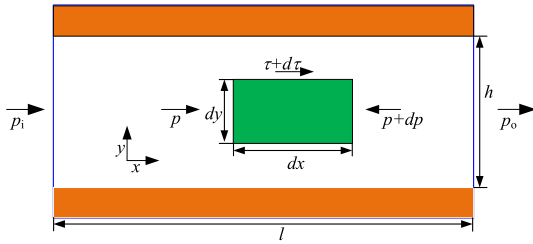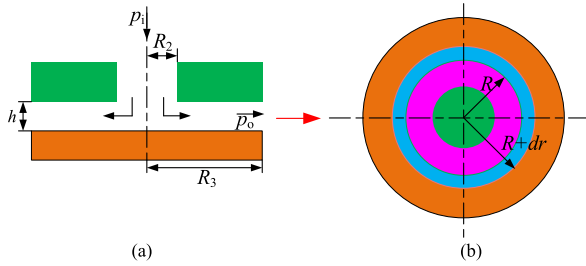
FIGURE 7. Parallel plate model.

FIGURE 8. Parallel disk model: (a) cross-section view and (b) front view.

FIGURE 9. Equivalent schematic of the conical MR fluid channel: (a) cross-section view and (b) equivalent model.

of MR fluid, and h is the gap between the upper plate and lower one.

The flow rate q is

$$q = \int_h^0 uA = \int_h^0 2\pi\, budy = \frac{\pi bh^3}{6\eta l}\Delta p \quad (21)$$

where b is the unfolded width of MR fluid.

Based on the Bingham model, the pressure drop Δp can be expressed as

$$\Delta p = \Delta p_\eta + \Delta p_\tau = \frac{12\eta q}{bh^3}l + \frac{c\tau_y}{h}l \quad (22)$$

where τ_y is the yield stress of MR fluid.

Therefore, the viscosity pressure drop $\Delta p_{a-\eta}$ and field-dependent pressure drop $\Delta p_{a-\tau}$ in the annular fluid channels can be expressed as

$$\Delta p_{a-\eta} = \Delta p_{1-\eta} + \Delta p_{2-\eta} + \Delta p_{3-\eta} = \frac{12\eta Av}{bh_1^3}W \quad (23)$$

$$\Delta p_{a-\tau} = \Delta p_{1-\tau} + \Delta p_{3-\tau} = \frac{c\tau_3}{h_1}(w_1 + w_2) \quad (24)$$

where A is the piston area, v is the piston velocity, c is the correctional factor, and τ_3 denotes the yield stress of the MR fluid in paths I and III.

Supposing the conical gap is similar to a parallel disk gap, the pressure drop in the conical fluid channels can be determined via the parallel disk model as depicted in Fig. 8. Based on the parallel disk model [30], the flow rate q can be calculated as

$$q = \frac{\pi R\tau_y}{6\eta(\frac{dp}{dr})^2}[(4\tau_y^3 - 3\tau_y h^2(\frac{dp}{dr})^2 - h^3(\frac{dp}{dr})^3] \quad (25)$$

where R means the parallel disk radius, dr is the unit radius of the parallel disk, and dp is the pressure drop in dr.
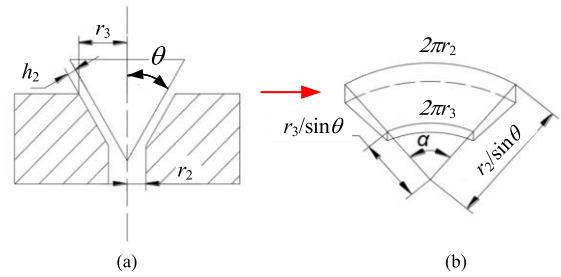
In view of Equation (25), it can be obtained as follows

$$(\frac{dp}{dr})^3 + (\frac{3\tau_y}{h} + \frac{6\eta q}{\pi Rh^3})(\frac{dp}{dr})^2 - 4(\frac{\tau_y}{h})^3 = 0 \quad (26)$$

Similarly, the pressure drop of the parallel disk model can be expressed as

$$\Delta p = \Delta p_\eta + \Delta p_\tau = \frac{6\eta q}{\pi h^3}\ln\frac{R_2}{R_3} + \frac{c\tau_y}{h}(R_2 - R_3) \quad (27)$$

where R_2 and R_3 represent the maximum and minimum radius of the parallel disk as shown in Fig. 8, respectively.

By unfolding the conical fluid channels shown in Fig. 9, the half core angle α of the extended surface can be calculated as

$$\alpha = 2\pi\sin\theta \quad (28)$$

Accordingly, the viscosity pressure drop $\Delta p_{c-\eta}$ and field-dependent pressure drop $\Delta p_{c-\tau}$ in the annular fluid channels can be deduced as

$$\Delta p_{c-\eta} = \Delta p_{4-\eta} + \Delta p_{5-\eta} + \Delta p_{6-\eta} = \frac{6\eta Av}{\pi\sin\theta h_2^3}\ln\frac{r2}{r3} \quad (29)$$

$$\Delta p_{c-\eta} = \Delta p_{4-\eta} + \Delta p_{6-\eta} = \frac{c(\tau_1 w_1 + \tau_2 w_2)}{h_2\cos\theta} \quad (30)$$

where τ_1 and τ_2 denote the yield stress of the MR fluid in paths IV and VI, respectively.

The total pressure drop Δp of the proposed MR damper can be obtained as

$$\Delta p = \frac{12\eta Av}{bh_1^3}W + \frac{6\eta Av}{\pi\sin\theta h_2^3}\ln\frac{r2}{r3} + \frac{c\tau_3}{h_1}(w_1 + w_2) + \frac{c(\tau_1 w_1 + \tau_2 w_2)}{h_2\cos\theta} \quad (31)$$

Observing equation (31), the total pressure drop Δp includes four terms; the first two terms called viscosity pressure drop coming from the uncontrollable part which is related to the specific structure of the MR damper, and the latter two terms derived from the field-dependent part which is entirely relied on the applied magnetic field controlled by a direct current.

Thus, the output damping force of the proposed MR damper is represented as

$$F = \Delta pA = F_\eta + F_\tau \quad (32)$$

where F_η and F_τ represent the viscosity damping force and field-dependent damping force, respectively.

The dynamic range K of the proposed MR damper is defined as the ratio of F to F_η:

$$K = \frac{F}{F_\eta} = 1 + \frac{F_\tau}{F_\eta} \qquad (33)$$

IV. SIMULATION ANALYSIS USING THE FEA METHOD

A. MODELING OF THE PROPOSED MR DAMPER

To validate the structural feasibility of the proposed MR damper with enhanced effective gap lengths, the FEA method was conducted by using ANSYS/Emag software (version 17.0). The FEA in which the magnetic field is produced by the excitation coil can be modeled via static electromagnet simulation without considering the effect of piston velocity on changing the distribution of magnetic field. In fact, the piston velocity exerts a little effect on the distribution of magnetic field in effective gaps. Firstly, a 2-D finite element model of the proposed MR damper was constructed as depicted in Fig. 10. It mainly consists of the valve spool, non-magnetic sleeves, magnetic yokes, excitation coil, conical sleeve, piston rod, and cylinder. Among them, valve spool, magnetic yokes, and cylinder are made from 10# steel with a high magnetic permeability, whose B-H property is depicted in Fig. 11. Here, the MR fluid adopts MRF-J01T provided by the Chongqing Instrument Material Research Institute in China; its magnetic properties are defined by τ–B curve and B-H curve, as shown in Fig. 12. Non-magnetic sleeves, conical sleeve, and piston rod are made from the stainless steel with a relative permeability of 1; the excitation coil is made of copper which possesses a relative permeability of 1 as well. After meshing grid and assigning material areas, the input current was loaded and the boundary constraint of magnetic flux lines was specified. Finally, the solving procedure was processed.
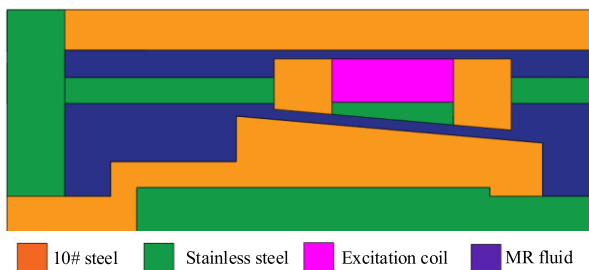
FIGURE 10. Finite element model of the proposed MR damper.

Observing Fig. 12a, the relationship between τ and B can be confirmed using the least square method to the cubic polynomial fitting of MRF-J01T, which is expressed as:

$$\tau_y = a_1 \times B^3 + a_2 \times B^2 + a_3 \times B + a_4 \qquad (34)$$

where a_0, a_1, a_2 and a_3 respectively denote polynomial coefficients, here $\alpha_1 = -984.27$ kPa/T^3, $\alpha_2 = 865.39$ kPa/T^2, $\alpha_3 = -48.46$ kPa/T, and $\alpha_4 = 0.018$ kPa [32].
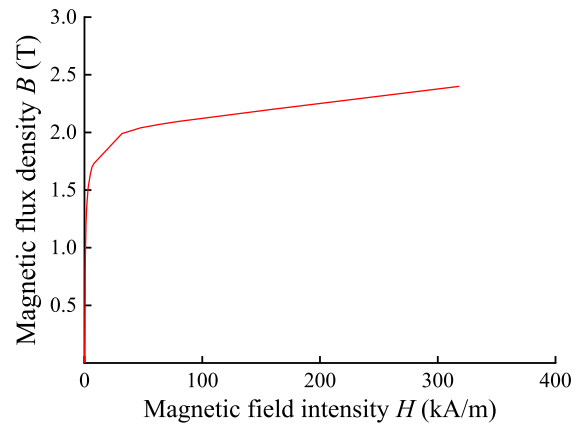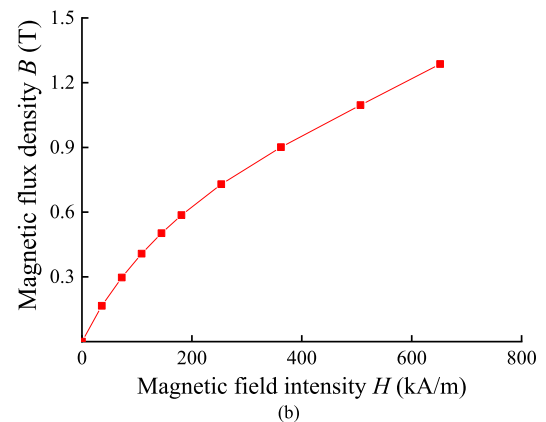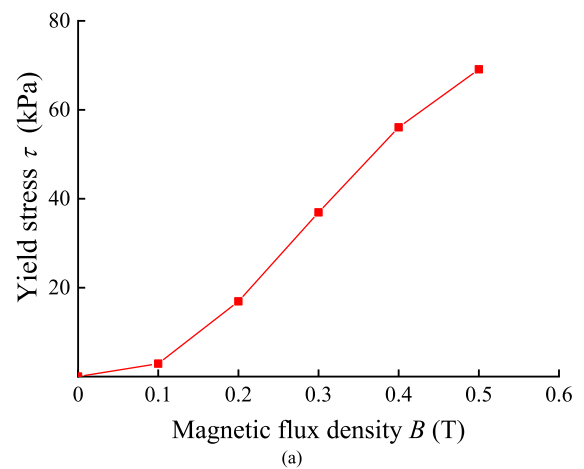
FIGURE 11. *B-H* curve of 10# steel.

FIGURE 12. Magnetic properties of MR fluid: (a) $\tau - B$ curve and (b) *B-H* curve.

B. SIMULATION ANALYSIS

Fig. 13 represents the magnetic flux lines distribution of the proposed MR damper at applied current of 1 A, where the adjustable gap in the conical fluid channels is fixed at 1 mm. In general, the magnetic flux lines are intensively distributed in the primary magnetic circuits. However, there is a proportion of magnetic leakage which exists at the non-magnetic

sleeves, owing to the permeability superiority of 10# steel over MR fluid. On the other hand, it is found that magnetic field lines are distributed centrally around the excitation coil, and magnetic flux lines in magnetic yokes are denser than that in other regions. Moreover, the magnetic flux lines nearly vertically pass through the effective gaps in the annular and conical fluid channels.
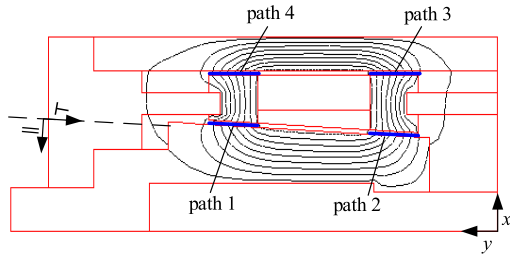

FIGURE 13. **Distribution of magnetic flux lines.**

Fig. 14 reveals the magnetic flux density contour of the proposed MR damper. Here, the color depth indicates the value of magnetic flux density. As shown in Fig. 14, the magnetic flux densities in effective gaps are relatively higher than that in other regions, which is consistent with the distribution of magnetic flux lines as portrayed in Fig. 13. In addition, the maximum magnetic flux density intensively located at path 1 is greater than that in path 3 and path 4, indicating that the conical fluid channels play an important role in the design of the proposed MR damper. Thereby, it can be preliminarily verified that the dynamic performance of the proposed MR damper can be obviously enhanced by compactly integrating the conical fluid channels into the annular MR channels.
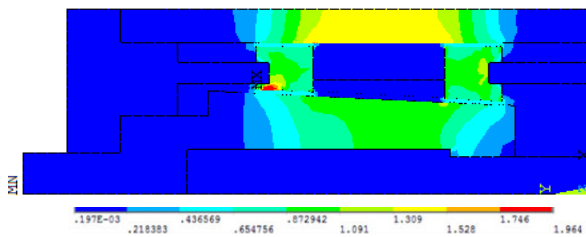

FIGURE 14. **Contour of magnetic flux density.**

The magnetic flux density along path 3, i.e. B_x, is essentially identical to that along path 4, due to the structural symmetry of the annular MR fluid channel as shown in Fig. 14. Nevertheless, the magnetic flux densities along path 1 and path 2 are not precisely coincident with the x-direction or y-direction. Thus, the coordinate transformation is implemented to convert them into the directions vertical parallel to path 1 and path 2, it can be expressed as:

$$B_\perp = B_x \cos\theta - B_y \sin\theta \tag{35}$$
$$B_\parallel = B_x \sin\theta + B_y \cos\theta \tag{36}$$

where B represents the magnetic flux density parallel to the path 1 and path 2, $B_\perp$ represents the magnetic flux density

perpendicular to path 1 and path 2, and B_x and B_y are the magnetic flux density along x-direction and y-direction, respectively.

Fig. 15a shows the distribution of magnetic flux density at the adjustable gaps along path 1. As portrayed in Fig. 15a, the magnetic flux density $B_\perp$ perpendicular to the effective gap is basically stable at −0.52 T, where the negative symbol represents that the magnetic flux density direction is opposite to the given direction. The magnetic flux density $B_\parallel$ parallel to the effective gap is slightly zero, which greatly attributes that the magnetic flux lines can almost vertically pass through the adjustable gaps. On the other hand, the magnetic flux density varies sharply at the position of 0 mm and 13 mm in path 1, this is because the magnetic flux lines did not vertically pass through the adjustable gaps.
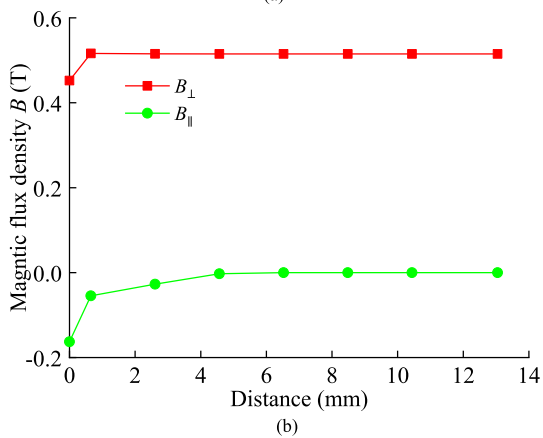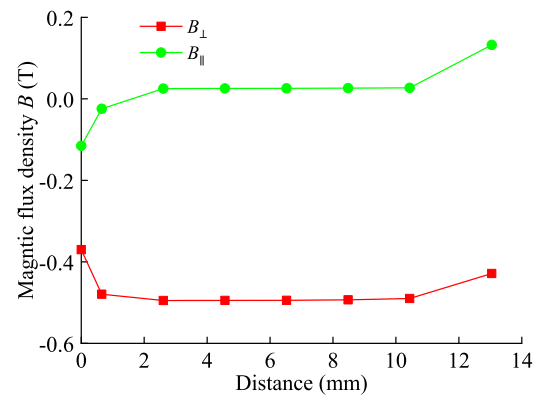

FIGURE 15. **Distribution of magnetic flux densities along different paths: (a) path 1 and (b) path 2.**

Fig. 15b displays the distribution of magnetic flux density at the adjustable gaps along path 2. Similarly to Fig. 15a, the magnetic flux density $B_\perp$ that is perpendicular to the adjustable gaps primarily remains 0.51 T, the magnetic flux density $B_\parallel$ parallel to the effective gaps is nearly zero. Nevertheless, magnetic flux density $B_\perp$ in path 1 is slightly higher than that in path 2, owing to the denser magnetic flux lines distributed in path 1 than that in path 2.

Fig. 16a and Fig. 16b reveal the relationship between magnetic flux densities and applied current in path 1 and
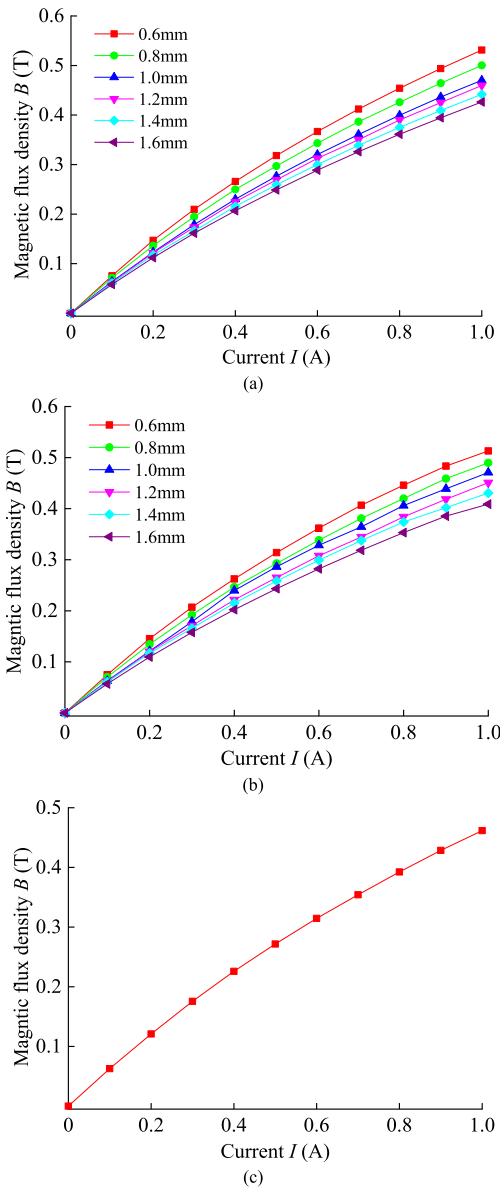
FIGURE 16. Magnetic flux densities along different paths: (a) path 1, (b) path 2 and (c) path 3 and path 4 at the adjustable gap of 1.0 mm.

path 2 with the adjustable gaps ranging from 0.6 mm to 1.6 mm, respectively. It can be found the magnetic flux density increases with the increase of the applied current, but decreases as the adjustable gaps increase in the longitudinal direction. This is because reducing the adjustable gaps decreases the resistance of the MR fluid in path 1 and path 2, which gives rise to the promotion of the magnetic flux density. Specifically, the magnetic flux density changes prominently around the adjustable gap of 1 mm. On the other hand, the magnetic flux density in path 1 is slightly greater than that in path 2 at the identical gap and applied current.

Fig. 16c illustrates the relationship between the magnetic flux density and applied current in path 3 and path 4 at the adjustable gap of 1.0 mm. The magnetic flux density in path 3 and path 4 reaches about 0.43 T at the applied current of 1 A,

which is slightly less than that in path 1 and path 2 at the adjustable gap fixed at 1 mm.

Fig. 17 illustrates the variation of the damping force and Fig. 18 displays the distribution of damping force under different applied currents and adjustable gaps, where the piston velocity is fixed at 25.12 mm/s. The damping force increases by increasing the applied current and reducing the adjustable gaps. It is noted that the increasing tendency of the damping force emerges smoothly at the applied current larger than 0.8 A and the adjustable gaps greater than 1.2 mm, owing to the saturation phenomenon of the magnetic circuit. Specifically, the regulating scope of the damping force under different gaps and applied currents ranges from 0.2 kN to 9.6 kN, which manifests the proposed MR damper has better dynamic performance compared with conventional MR dampers.
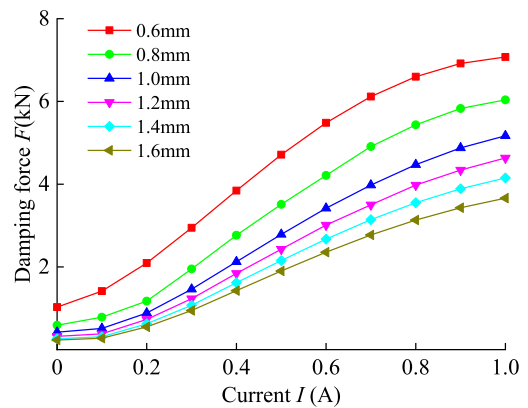

FIGURE 17. Variation of the damping force and current under different gaps at the piston velocity of 25.12 mm/s.
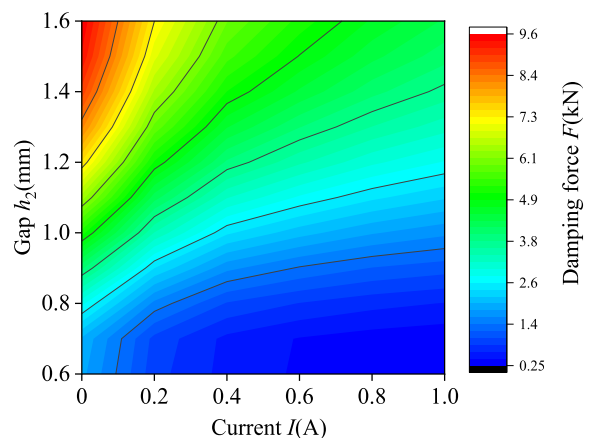

FIGURE 18. Distribution of the damping force and gap under different currents at the piston velocity of 25.12 mm/s.

V. DYNAMIC PERFORMANCE ANALYSIS
A. PROTOTYPE AND DYNAMIC TEST RIG
The experimental test rig is set up shown in Fig. 19. In this experiment, the dynamic test rig mainly consists of the DC power supply (PS-305D), Fatigue machine (WPL-50),

prototype of MR damper, data acquisition board, and PC (Intel i7–3.4 GHz processor and 8 GB of RAM). The MR damper was fixed on the Fatigue machine using a specific clamp. Fatigue machine was utilized to provide different kinds of displacement excitation, the DC power supply was applied to adjust the control current in the excitation coil, and the PC was adopted to collect experimental data via the data acquisition board.
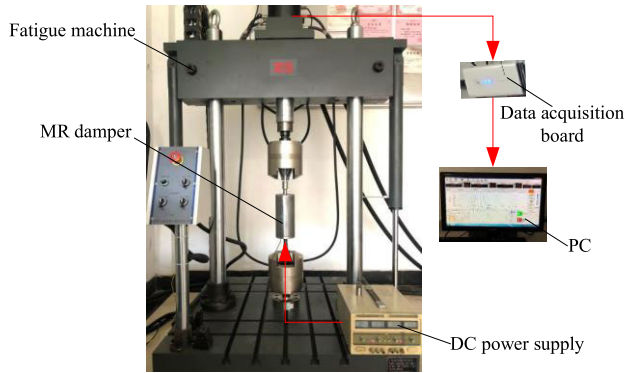

FIGURE 19. Experimental test rig of the proposed MR damper.

B. DYNAMIC PERFORMANCE AT AN ADJUSTABLE GAP OF 1.0 mm

By setting the displacement excitation with amplitude of 4 mm and frequency of 0.4 Hz, the damping force-displacement and damping force-velocity curves at the adjustable gap of 1 mm were obtained, as detailed in Fig. 20 and Fig. 21, respectively. It can be obviously found from Figs. 20 and 21 that the simulated damping force fits quietly well with experimental damping force under different displacement and velocity, thus demonstrating the correctness of the design theory. Observing Fig. 20, the growing trend of damping force is slightly associated with the increase of the displacement, indicating that there is no apparent relationship between the damping force and displacement. As depicted in Fig. 21, the damping force augments with the increment of the applied current at an optionally fixed velocity. The increasing tendency of damping force is gradually smooth, suggesting that the magnetic circuit smoothly approaches saturation. Furthermore, when the applied current remains unchanged, the damping force almost monotonously raises with enhancing the velocity. Specifically, the experimental damping force appears a peak of 4.3 kN at applied current of 1.0 A Nevertheless, the minimum damping force, namely the viscosity damping force, achieves only 0.3 kN at applied current of 0 A.

The damping force-displacement curve at an adjustable gap of 1mm was acquired, under the displacement excitation with frequency of 0.4 Hz and amplitudes of 4 mm, 6 mm, and 8 mm, as depicted in Fig. 22. It is apparent that the damping force exhibits a mild enhancement with the augmentation of the amplitude. This phenomenon directly results from that
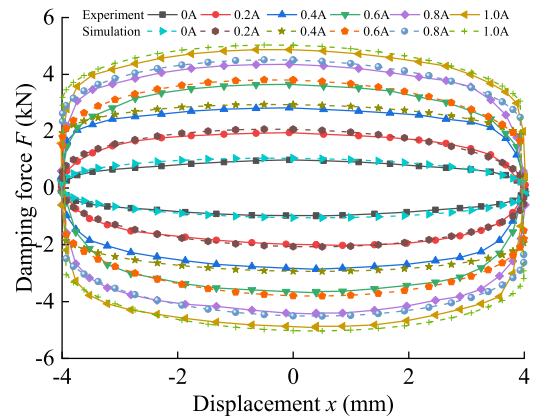

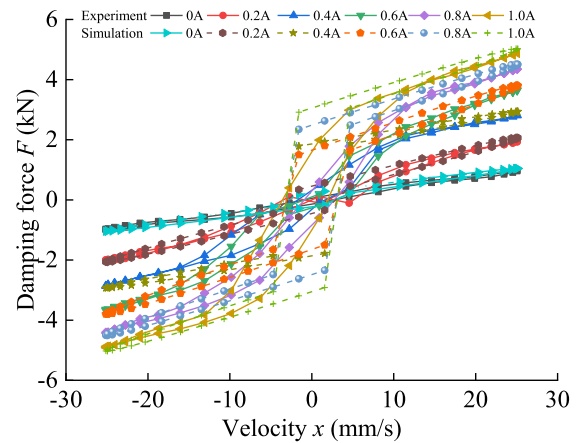**FIGURE 20.** Damping force versus displacement under different currents.

FIGURE 21. Damping force versus velocity under different currents.

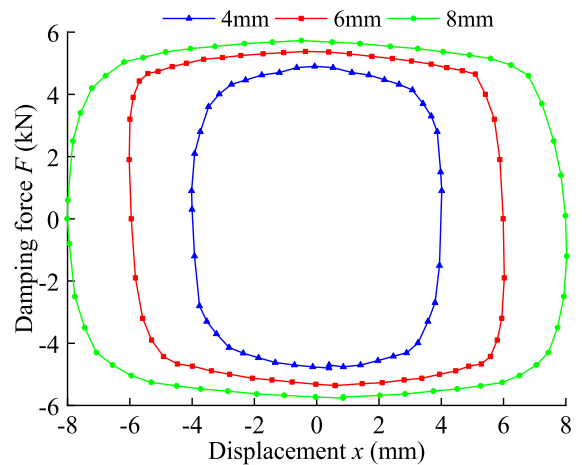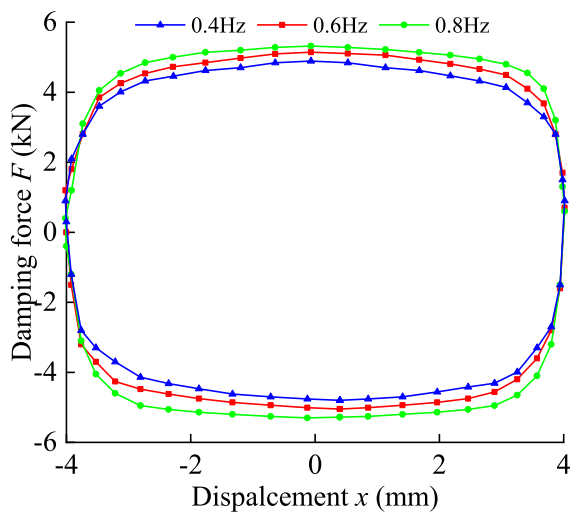**FIGURE 22.** Damping force versus displacement under amplitudes of 4, 6, 8 mm, respectively.

increasing the amplitude enlarges the velocity of the piston rod at a settled frequency. Therefore, the curve of the damping force manifests a slight increment. Additionally, the maximum damping force is identified with the values of 4.3 kN and 5.1 kN associated with the amplitudes of 4mm and 8mm, respectively.

When the MR damper was loaded under the displacement excitation with amplitude of 4 mm and frequencies of 0.4 Hz, 0.6 Hz, and 0.8 Hz, the damping force-displacement plot illustrated in Fig. 23 was obtained. Observing Fig. 23, the damping force grows up slowly as the frequency of excitation uniformly augments as well. This is the enhancement of frequency increases the damper velocity at an invariable amplitude; thus, the damping force increases mildly, which is similar to the occurrence of the damping force displayed in Fig. 22. Moreover, the maximum damping force gently reaches 4.3 kN at the frequency of 0.4 Hz, and the maximum damping force is up to 4.9 kN at the amplitude of 0.8 Hz, indicating that the frequency of the excitation signal plays a less crucial role in enlarging damping force.
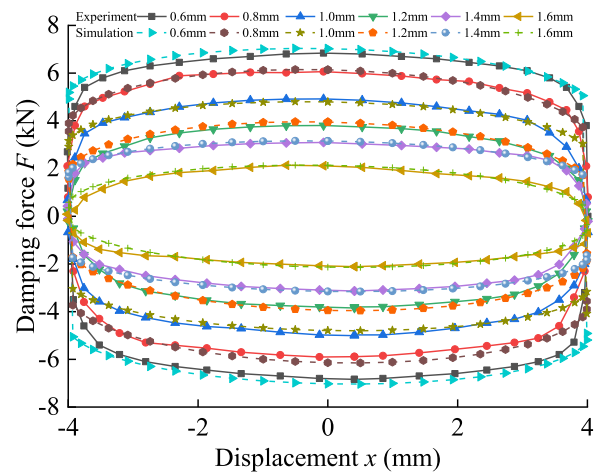

FIGURE 23. Damping force versus displacement under frequencies of 0.4, 0.6, 0.8 Hz, respectively.

From discussed above, it is obviously seen that both the frequency and amplitude of the excitation signal exert a little influence on controlling the damping force. Nevertheless, the applied current is one of the determining factors which greatly affect the damping force until the magnetic circuit ascends to saturation, verifying the effectiveness of controlling the current to achieve the continuous adjustment of damping force. As a highlight, the proposed MR damper with the adjustable gap of 1mm displays an expected damping performance, which achieves the damping force varying from 0.4 kN to 4.3 kN with applied currents of 0 A and 1.0 A, respectively. Hence, this MR damper with the adjustable gap of 1 mm can be served as a conventional MR damper featuring enhanced effective length, which obviously shares a better damping force compared with the most common used MR damper.

C. DYNAMIC PERFORMANCE WITH ADJUSTABLE GAPS RANGING FROM 0.6 mm TO 1.6 mm

In this part, a series of experiments of the proposed MR damper with different gaps were conducted to acquire a more

promising dynamic performance compared with the fixed gap of 1mm. By applying the displacement excitation with amplitude of 4 mm and frequency of 0.4 Hz, the damping force-gap curve was obtained as depicted in Fig. 24. It is noticeably revealed that both the experimental and simulated damping force uniformly decreases with the increase of the gap at a specified velocity. Concretely, the obvious tendency appears as the experimental gap rises from 0.6 mm to 1.2 mm, while the decreasing trend is relatively slow at the gap large than 1.2 mm. Specifically, the experimental damping force varies significantly at the gap of around 1 mm.
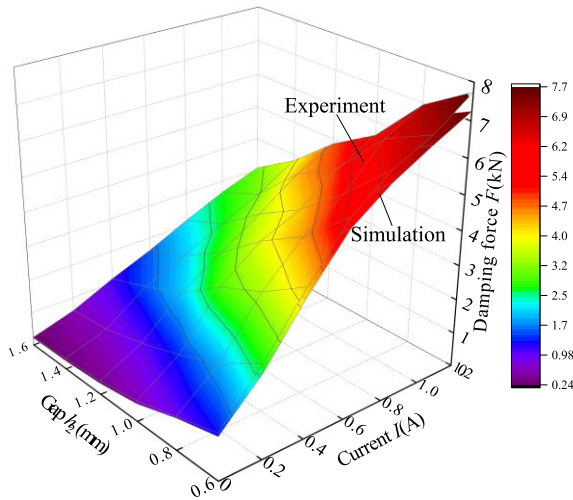

**FIGURE 24.** Damping force versus displacement with different adjustable gaps.

Fig. 25 depicts the dynamic variation of the experimental and simulated damping forces under different currents and adjustable gaps. It can be observed that both the experimental and simulated damping forces positively associate with the applied current while negatively correlate to the adjustable gap, whereas a little difference between the experimental and simulated damping forces occurs primarily due to the weakening rheological properties of the long-unused MR fluid and regulation precision of the adjustable gaps when conducted experiment. Specifically, the maximum experimental damping force appears with the applied current of 1.2 A and adjustable gap of 0.6 mm, while the minimum one occurs at applied current of 0 A and adjustable gap of 1.6 mm.

The relationship between the damping force and the adjustable gap was obtained as presented in Fig. 26 under sequentially applied currents from 0 A to 1.2 A with an interval of 0.2 A. According to Fig. 26, there exists a positive correlation between the damping force and current but the increasing tendency becomes slowly owing to the saturation phenomenon of the magnetic circuit. On the other hand, the damping force linearly associates the adjustable gap when the applied current basically remains unchanged.
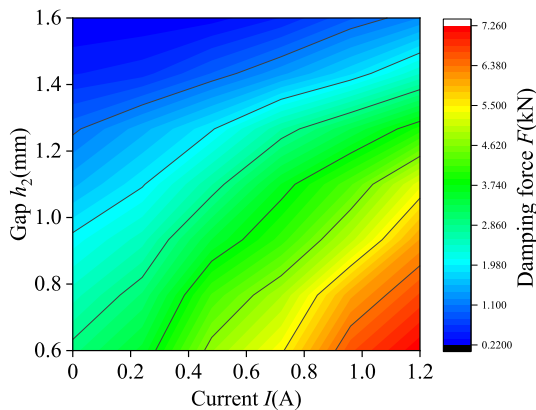
Figure 27 displays the distribution of damping force under different gaps and currents. The peak damping force appears at applied current of 1.2 A and adjustable gap of 0.6 mm while the minimum one occurs at applied current of 0 A

FIGURE 25. Dynamic variation of experimental and simulated damping forces under different currents and adjustable gaps.
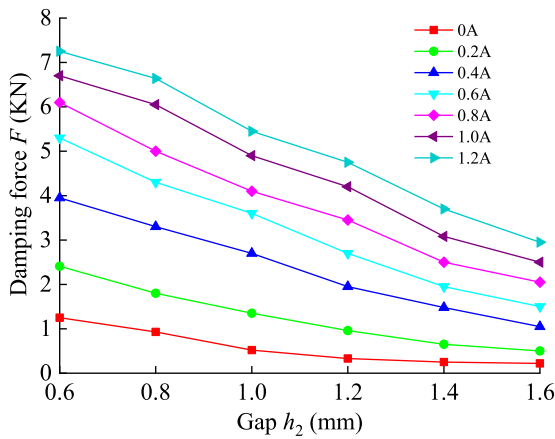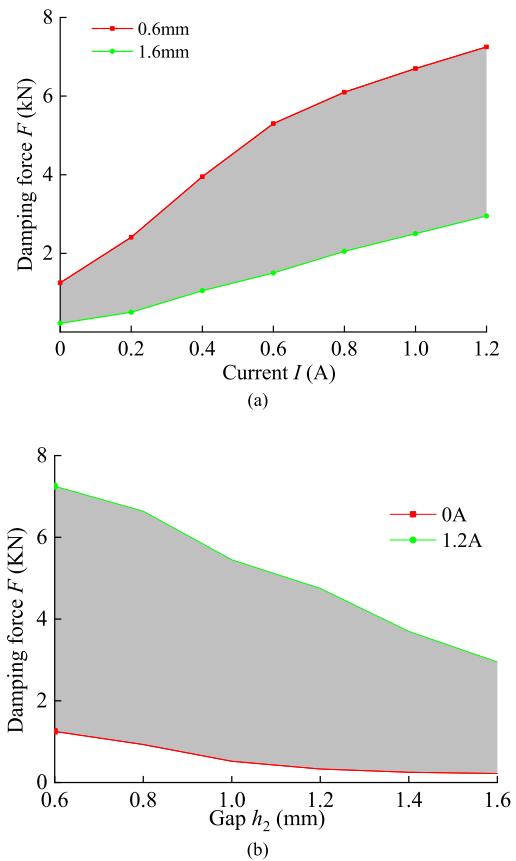

FIGURE 26. Damping force versus adjustable gap under different currents.

FIGURE 27. Distribution of damping force under different gaps currents.

Fig. 28 shows the regulating scope of the damping force at different currents and adjustable gaps. Note that the viscous damping force appears with the applied current of 0 A. Likewise, both the viscous damping force and field-dependent damping force decrease with the increase of the adjustable gap, while the field-dependent damping force increase as increasing the applied current. Moreover, the damping forces at applied current of 0 A, namely the viscous damping forces, respectively reach 0.2 kN and 1.3 kN. The maximum damping forces achieve 2.9 kN and 7.2 kN at an applied current of 1 A, respectively. Compared with the adjustable gap of 1 mm, the damping force with the adjustable gaps ranging from 0.6 mm to 1.6 mm exhibits an enhanced dynamic performance, whose damping force is approximately 1.4 times larger than that at the adjustable gap of 1 mm.

FIGURE 28. Regulating scope of the damping force: (a) damping force versus current and (b) damping force versus adjustable gap.

The dynamic variation of dynamic range under different currents and adjustable gaps is displayed in Fig. 29. It can be noticed that the dynamic range positively associates with the adjustable gap while negatively correlate to the applied current. Moreover, the experimental dynamic range corresponds well with the simulated one. The maximum dynamic range significantly reaches 33, appearing with the applied current of 0 A and adjustable gap of 1.6 mm, while the minimum one occurs at applied current of 1.2 A and adjustable gap of 0.6 mm.
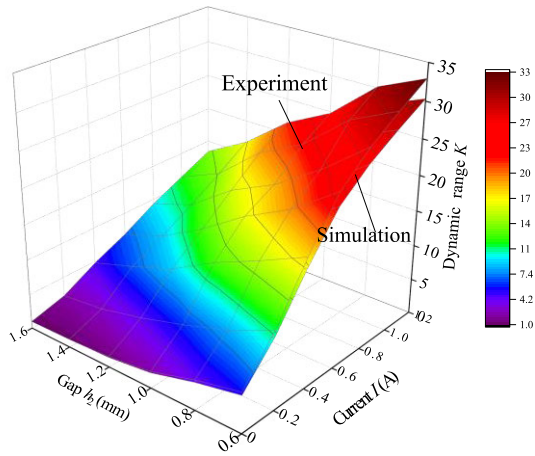
and adjustable gap of 1.6 mm. Nevertheless, the damping force undergoes a relatively mild augmentation as the applied current is larger than 0.8 A, which implies that the magnetic circuit approaches saturation slowly.

FIGURE 29. Dynamic variation of experimental and simulated dynamic range under different currents and adjustable gaps.
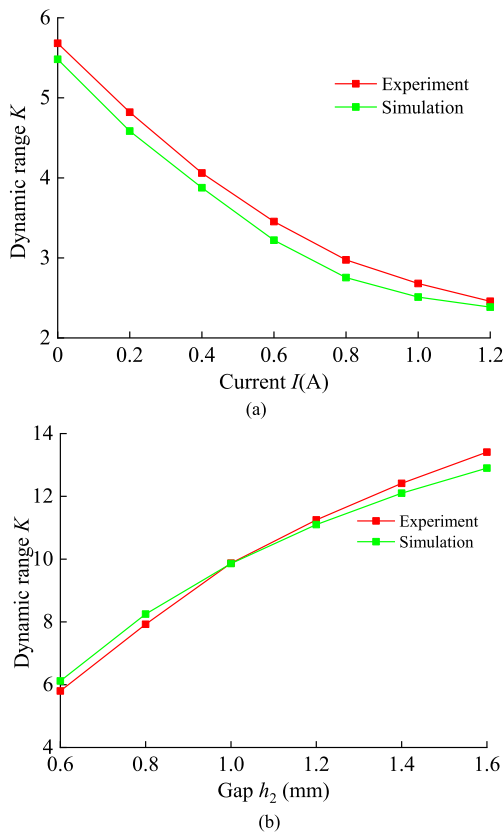

(a)

(b)

FIGURE 30. Regulating scope of the dynamic range: (a) dynamic range under different currents and (b) dynamic range under different gaps.

The regulating scope of the dynamic range depicted in Fig. 30 was experimentally and theoretically obtained. It can be noticed in Fig. 30a that the experimental dynamic range uniformly decreases as the applied current increases and this tendency is a little different compared with the simulated damping force depicted in Fig. 20a. Furthermore, the experimental dynamic range varies from 2.6 to 5.7 at the applied currents of 1.2 A and 0 A, respectively. Observing Fig. 30b, the dynamic range non-linearly increases with

the enlargement of the gap. Specifically, the experimental dynamic range attains 13.6 at the adjustable gap of 1.6 mm while the minimum one equal to 5.9 at the adjustable gap of 0.6 mm.

According to the damping force and dynamic range with the adjustable gaps, it can be found that the dynamic range decreases with the increment of the gap; nevertheless, the dynamic range increases with the increase of the adjustable gap. This phenomenon markedly reflects the enhancement of dynamic range decreases the damping force, which, in a large degree, inevitably appears for conventional MR dampers featuring fixed gaps, resulting in a lot of tedious and repetitive MR damper design for different conditions.

In order to verify the designed damping force under different applied currents and gaps, by adopting the current as sinusoidal excitation and velocity of 15.7 mm/s, the damping force control result is represented as Fig. 31. It can be observed that the damping force follows the control current at a fixed gap and the controlling damping force increases with the decrease of the adjustable gaps; meanwhile, from the damping force profile, it can be calculated by equation (33) that the proposed MR damper possesses a wider dynamic range, indicating that this MR damper can be well controlled by applied currents and the adjustable gaps.
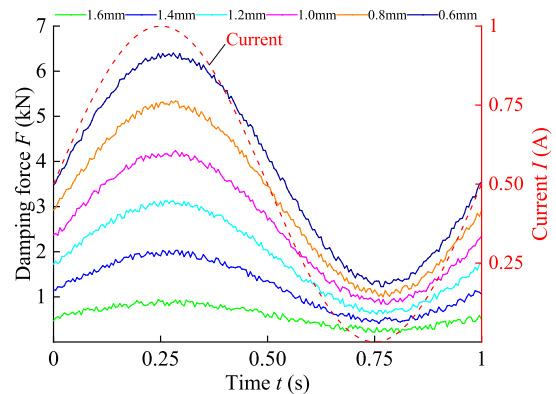

FIGURE 31. Control damping force under different currents and gaps.

The response time of the electromagnetic field is also one of the significant factors to assess the dynamic performance of the proposed MR damper. Herein, the response time experiment of the electromagnetic field under different adjustable gap was conducted, and the result is depicted in Fig. 32. It is noted that the time when the voltage attains 90% of steady voltage U_0 is defined as the response time of the electromagnetic field. The variation of voltage starts at 600 ms and it can be observed that the response times under different gaps are 19.8, 20.7, 21.3 22.4, 23.5, 24.2 ms, respectively, manifesting the rapid response of the proposed MR damper to control currents under different gaps.

It is noted that the structure size significantly influences the dynamic performance of MR dampers. Hence, the comparison between the proposed MR damper and other classic MR dampers is meaningless because the structure sizes of the
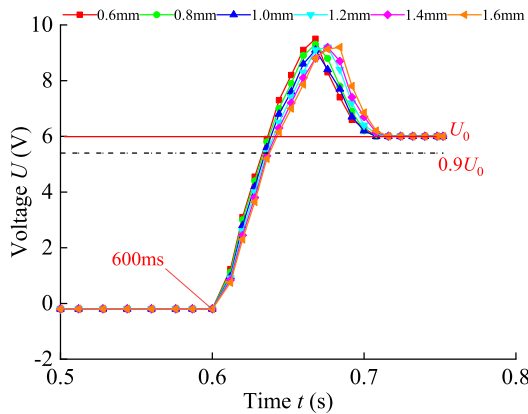
FIGURE 32. Response time of the electromagnetic field.

above MR dampers are not designed with the same structure size. Nevertheless, when the adjustable gap is fixed as 1 mm, the proposed MR damper can be served as a classic MR damper which has been successfully proposed and designed in literature. Therefore, the comparison between the proposed MR damper with adjustable gaps of 1 mm and conventional one is conducted, which is listed in Table 2. It can be noticed that the proposed MR damper with enhanced effective gap lengths achieves satisfactory goals. From a structural configuration perspective, the proposed MR damper achieves a double extension of the effective gap lengths via compactly integrating the conical fluid channels into the annular fluid channels. On the other hand, from the control strategy point of view, the damping force can be not only controlled by excitation current but also simultaneously altered by regulating the width of the adjustable gaps in the conical fluid channels. Hence, the MR damper designed in this paper can promisingly replace a variety of conventional MR dampers featuring fixed gaps, which vastly improve the dynamic performance of conventional MR dampers and further expand the application domains applied with MR dampers.

TABLE 2. Comparison between the proposed and conventional MR damper.

Indexes	Proposed	Conventional
Outer radius r	50 mm	50 mm
Stroke	±35 mm	±35 mm
Gap h_2	0.6-1.6 mm	1.0 mm
Magnetic flux density B (path 1)	0.41-0.53 T	0.46 T
Magnetic flux density B (path 2)	0.39-0.52 T	0.44 T
Respond time t	21.1 ms	21.3 ms
Damping force F	7.2 kN	4.6 kN
Dynamic range K	33	9.8
Control type	Current/gap	Current
Adaptability	flexible	simple

VI. CONCLUSION

The proposed MR damper with enhanced effective gap lengths can alter the relative position between the valve spool

and piston by adjusting the locking nut; therefore, the gap in the conical fluid channels can be continuously adjusted. Meanwhile, the proposed MR damper can achieve a double extension of effective gap lengths via compactly integrating the conical fluid channels into the annular fluid channels.

The experimental results show that the damping force decrease with the increment of the adjustable gap under a fixed applied current, and the maximum damping force comes up to 7.2 kN at the adjustable gap of 0.6 mm. Moreover, the dynamic range increases with increasing the width of adjustable gaps, and the dynamic range appears with a peak of 13.6.

The damping force and dynamic range can be not only effectively controlled by excitation current but also flexibly altered by regulating the width of the adjustable gap simultaneously. Compared with the dynamic performance of the conventional MR damper featuring fixed gap (the damping force and dynamic range only reach 5.7 kN and 9.6, respectively), the damping force of the proposed MR damper varies from 0.2 kN to 7.2 kN and the dynamic range attains 33 correspondingly. Thus, the dynamic performance of the proposed MR damper is significantly enhanced.

REFERENCES

[1] R. Jeyasenthil, D. S. Yoon, and S.-B. Choi, "Response time effect of magnetorheological dampers in a semi-active vehicle suspension system: Performance assessment with quantitative feedback theory," *Smart Mater. Struct.*, vol. 28, no. 5, May 2019, Art. no. 054001.

[2] T.-H. Lee, C. Han, and S.-B. Choi, "Design and damping force characterization of a new magnetorheological damper activated by permanent magnet flux dispersion," *Smart Mater. Struct.*, vol. 27, no. 1, Jan. 2018, Art. no. 015013.

[3] L. Xu and Q. Fu, "Design and development of a Rayleigh oscillator-based reference angle generator for motion control of smart prosthetic knees," *IEEE Access*, vol. 8, pp. 32421–32431, 2020.

[4] L. Balamurugan, J. Jancirani, and M. A. Eltantawie, "Generalized magnetorheological (MR) damper model and its application in semi-active control of vehicle suspension system," *Int. J. Automot. Technol.*, vol. 15, no. 3, pp. 419–427, Apr. 2014.

[5] M. Wang, Z. Chen, and N. M. Wereley, "Magnetorheological damper design to improve vibration mitigation under a volume constraint," *Smart Mater. Struct.*, vol. 28, no. 11, Nov. 2019, Art. no. 114003.

[6] T. Oba, H. Kadone, M. Hassan, and K. Suzuki, "Robotic ankle–foot orthosis with a variable viscosity link using MR fluid," *IEEE/ASME Trans. Mechatronics*, vol. 24, no. 2, pp. 495–504, Apr. 2019.

[7] W. Cao, H. Yu, W. Chen, Q. Meng, and C. Chen, "Design and evaluation of a novel microprocessor-controlled prosthetic knee," *IEEE Access*, vol. 7, pp. 178553–178562, 2019.

[8] M. Wei, X. Rui, W. Zhu, F. Yang, L. Gu, and H. Zhu, "Design, modelling and testing of a novel high-torque magnetorheological damper," *Smart Mater. Struct.*, vol. 29, no. 2, Feb. 2020, Art. no. 025024.

[9] X.-X. Bai, S. Shen, N. M. Wereley, and D.-H. Wang, "Controllability of magnetorheological shock absorber: I. insights, modeling and simulation," *Smart Mater. Struct.*, vol. 28, no. 1, Jan. 2019, Art. no. 015022.

[10] X. Tang, D. Ning, H. Du, W. Li, Y. Gao, and W. Wen, "A Takagi–Sugeno fuzzy model-based control strategy for variable stiffness and variable damping suspension," *IEEE Access*, vol. 8, pp. 71628–71641, 2020.

[11] C. Khazoom, C. Veronneau, J.-P.-L. Bigue, J. Grenier, A. Girard, and J.-S. Plante, "Design and control of a multifunctional ankle exoskeleton powered by magnetorheological actuators to assist walking, jumping, and landing," *IEEE Robot. Autom. Lett.*, vol. 4, no. 3, pp. 3083–3090, Jul. 2019.

[12] K. Kim, Z. Chen, D. Yu, and C. Rim, "Design and experiments of a novel magneto-rheological damper featuring bifold flow mode," *Smart Mater. Struct.*, vol. 25, no. 7, Jul. 2016, Art. no. 075004.

[13] C. R. Liao, D. X. Zhao, L. Xie, and Q. Liu, "A design methodology for a magnetorheological fluid damper based on a multi-stage radial flow mode," *Smart Mater. Struct.*, vol. 21, no. 8, Aug. 2012, Art. no. 085005.

[14] R. Zemp, J. C. de la Llera, H. Saldias, and F. Weber, "Development of a long-stroke MR damper for a building with tuned masses," *Smart Mater. Struct.*, vol. 25, no. 10, Oct. 2016, Art. no. 105006.

[15] S. Zhu, L. Tang, J. Liu, X. Tang, and X. Liu, "A novel design of magnetorheological damper with annular radial channel," *Shock Vib.*, vol. 26, no. 3, 2016, Art. no. 8086504.

[16] I. I. M. Yazid, S. A. Mazlan, T. Kikuchi, H. Zamzuri, and F. Imaduddin, "Design of magnetorheological damper with a combination of shear and squeeze modes," *Mater. Des.*, vol. 54, no. 1, pp. 87–95, 2014.

[17] S. Seid, S. Chandramohan, and S. Sujatha, "Optimal design of an MR damper valve for prosthetic knee application," *J. Mech. Sci. Technol.*, vol. 32, no. 6, pp. 2959–2965, Jun. 2018.

[18] M. Cheng, Z. B. Chen, and J. W. Xing, "Design, analysis, and experimental evaluation of a magnetorheological damper with meandering magnetic circuit," *IEEE Trans. Magn.*, vol. 54, no. 5, pp. 1–10, May 2018.

[19] G. L. Hu, H. Liu, and J. Duan, "Damping performance analysis of MR damper with serial-type flow channel," *Adv. Mech. Eng.*, vol. 11, no. 1, pp. 1–12, 2019.

[20] T.-H. Lee and S.-B. Choi, "On the response time of a new permanent magnet based magnetorheological damper: Experimental investigation," *Smart Mater. Struct.*, vol. 28, no. 1, Jan. 2019, Art. no. 014001.

[21] G. Li and Z.-B. Yang, "Modelling and analysis of a magnetorheological damper with nonmagnetized passages in piston and minor losses," *Shock Vib.*, vol. 30, no. 3, pp. 1–12, 2020.

[22] X. Wu, C. Huang, Z. Tian, and J. Ji, "Development of a novel magnetorheological fluids transmission device for high-power applications," *Smart Mater. Struct.*, vol. 28, no. 5, May 2019, Art. no. 055021.

[23] Q. H. Nguyen, S. B. Choi, Y. S. Lee, and M. S. Han, "Optimal design of high damping force engine mount featuring MR valve structure with both annular and radial flow paths," *Smart Mater. Struct.*, vol. 22, no. 11, Nov. 2013, Art. no. 115024.

[24] G. L. Hu, Q. J. Liu, and R. Q. Ding, "Vibration control of semi-active suspension system with magnetorheological damper based on hyperbolic tangent model," *Adv. Mech. Eng.*, vol. 9, no. 5, pp. 1–15, 2017.

[25] S. H. Mousavi and H. Sayyaadi, "Optimization and testing of a new prototype hybrid MR brake with arc form surface as a prosthetic knee," *IEEE/ASME Trans. Mechatronics*, vol. 23, no. 3, pp. 1204–1214, Jun. 2018.

[26] J. Zheng, Y. Li, and J. Wang, "Design and multi-physics optimization of a novel magnetorheological damper with a variable resistance gap," *Proc. Inst. Mech. Eng. C, J. Mech. Eng. Sci.*, vol. 231, no. 17, pp. 3152–3168, Sep. 2017.

[27] W.-L. Song, D.-H. Li, Y. Tao, N. Wang, and S.-C. Xiu, "Simulation and experimentation of a magnetorheological brake with adjustable gap," *J. Intell. Mater. Syst. Struct.*, vol. 28, no. 12, pp. 1614–1626, Jul. 2017.

[28] D. X. Phu, K. Shah, and S.-B. Choi, "A new magnetorheological mount featured by changeable damping gaps using a moved-plate valve structure," *Smart Mater. Struct.*, vol. 23, no. 12, Dec. 2014, Art. no. 125022.

[29] W. H. Kim, J. H. Park, S. Kaluvan, Y.-S. Lee, and S.-B. Choi, "A novel type of tunable magnetorheological dampers operated by permanent magnets," *Sens. Actuators A, Phys.*, vol. 255, no. 1, pp. 104–117, Mar. 2017.

[30] G. Hu, M. Long, L. Yu, and W. Li, "Design and performance evaluation of a novel magnetorheological valve with a tunable resistance gap," *Smart Mater. Struct.*, vol. 23, no. 12, Dec. 2014, Art. no. 127001.

[31] X. X. Bai, W. Hu, and N. M. Wereley, "Magnetorheological damper utilizing an inner bypass for ground vehicle suspensions," *IEEE Trans. Magn.*, vol. 49, no. 7, pp. 3422–3425, Jul. 2013.

[32] G. Hu, J. Zhang, F. Zhong, and L. Yu, "Performance evaluation of an improved radial magnetorheological valve and its application in the valve controlled cylinder system," *Smart Mater. Struct.*, vol. 28, no. 4, Apr. 2019, Art. no. 047003.

GUOLIANG HU received the Ph.D. degree from Zhejiang University, China, in 2006. He is currently a Professor with East China Jiaotong University and the Director of the Key Laboratory of Conveyance and Equipment, Ministry of Education, East China Jiaotong University. He is involved in the projects sponsored by the National Natural Science Foundation of China and by the Natural Science Foundation of Jiangxi Province. He has published more than 100 technical articles in refereed international journals and conferences. His research interests include smart materials and structures, and fluid power transmission and control.

FENG YI is currently pursuing the M.S. degree with the School of Mechatronics and Vehicle Engineering, East China Jiaotong University. His research interest includes design and evaluation of magnetorheological damper with enhanced damping lengths.

WANG TONG is currently pursuing the M.S. degree with the School of Mechatronics and Vehicle Engineering, East China Jiaotong University. His research interest includes development and performance analysis of magnetorheological damper with adjustable damping gaps.

LIFAN YU received the B.Sc. and M.Sc. degrees in mechanical engineering from East China Jiaotong University, in 2011 and 2014, respectively. He is currently a Laboratory Staff with the School of Mechatronics and Vehicle Engineering, East China Jiaotong University. His research interest includes design, simulation, and experimental verifications of new magnetorheological valve.

• • •